iScience

CellPress
OPEN ACCESS

Article

Regulating thermochemical redox temperature via oxygen defect engineering for protection of solar molten salt receivers

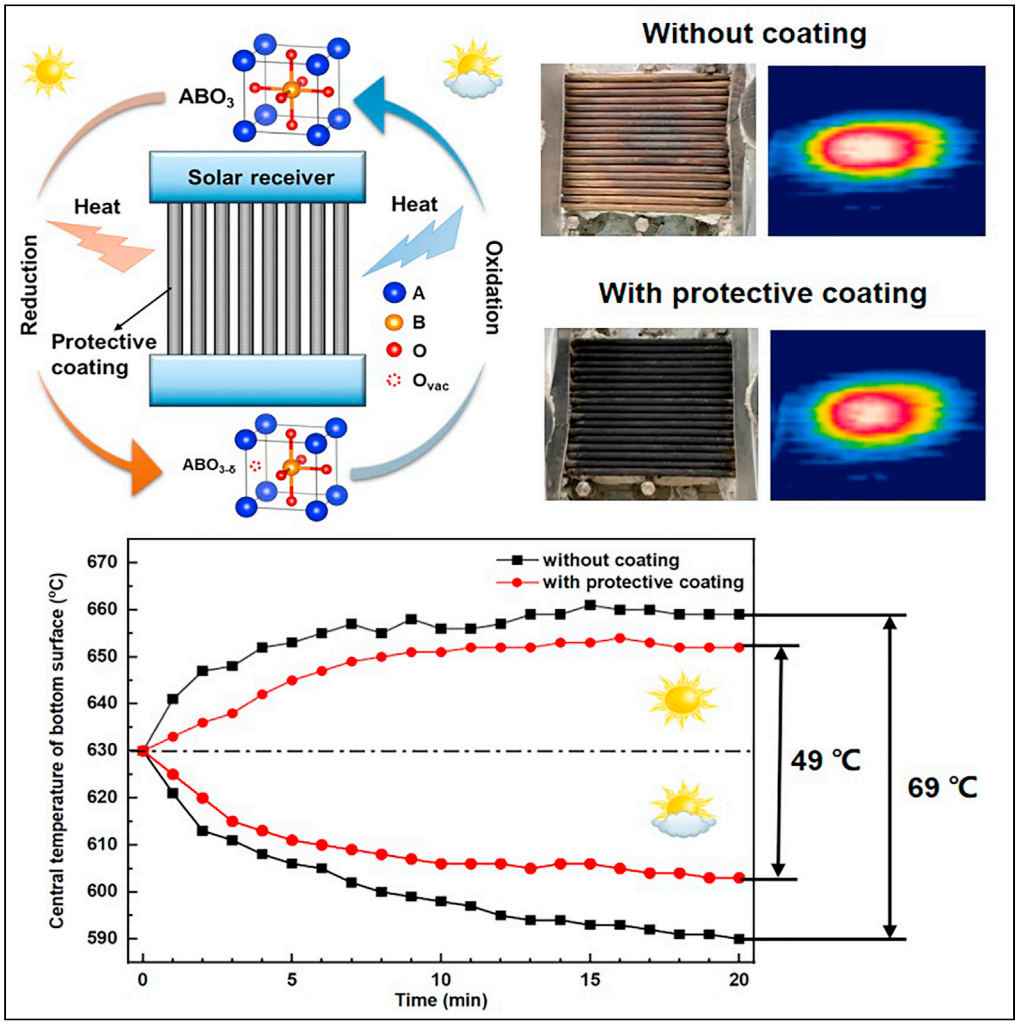

Peng Yuan, Changdong Gu, Haoran Xu, Zeyu Ning, Kefa Cen, Gang Xiao

xiaogangtianmen@zju.edu.cn

Highlights

A thermochemical protective coating for solar molten salt receivers is proposed

$BaCo_{1-x}Mn_xO_{3-\delta}$ (x = 0–0.4) materials show a good cyclability after 120 cycles

Thermochemical redox temperatures are regulated by oxygen defect engineering

$BaCo_{0.8}Mn_{0.2}O_{3-\delta}$ coating effectively relieves the thermal shock of the receiver

Yuan et al., iScience 24, 103039
September 24, 2021 © 2021 The Authors.
https://doi.org/10.1016/j.isci.2021.103039

iScience

CellPress
OPEN ACCESS

Article

Regulating thermochemical redox temperature via oxygen defect engineering for protection of solar molten salt receivers

Peng Yuan,[1,2] Changdong Gu,[3] Haoran Xu,[1,2] Zeyu Ning,[1,2] Kefa Cen,[1,2] and Gang Xiao[1,2,4,*]

SUMMARY

An active coating based on thermochemical redox reactions is proposed to protect molten salt receivers from solar flux fluctuation. However, appropriate metal oxides working in the temperature range of 530 and 850°C are still missing. Herein, we put forward an oxygen defect engineering strategy to regulate the thermochemical redox temperatures of perovskites. A tunable temperature range of 426–702°C is obtained by $BaCo_{1-x}Mn_xO_{3-\delta}$ ($x = 0$–0.4). It is found that a raised redox temperature can be obtained with the increase of the oxygen vacancy formation energy. For application, $BaCo_{0.8}Mn_{0.2}O_{3-\delta}$ is designed as the active protective coating of a lab-scale receiver, which has a thermal capacity of 82.95 kJ kg^{-1}. The smart coating can slow down the temperature rising rate from 8.5°C min^{-1} to 3°C min^{-1} in the first 2 min under strong solar radiation, effectively relieving the thermal shock of the receiver.

INTRODUCTION

Concentrated solar power (CSP) is expected to play an important role in relieving the current energy shortage and environmental degradation. By 2020, the global installed capacity of CSP has reached 6475MW, showing a significant acceleration (IRENA, 2021). CSP converts concentrated solar energy into thermal energy and then further into electricity through thermodynamic cycles. The four main types of CSP systems are parabolic trough systems, linear Fresnel systems, parabolic dish systems and power tower systems (Lewis, 2016). Parabolic trough systems and linear Fresnel systems have low concentration ratios, which only provide low working temperatures (under 400°C). Parabolic dish systems are mainly used for distributed energy generation. Compared with the above-mentioned systems, power tower systems are especially attractive because of the high concentration ratio and the simple cycle structure. A typical solar tower power plant is mainly composed of a heliostat field, a central receiver, a storage system, and a power generation system (Carrillo et al., 2019). Among these components, the receiver is an indispensable device which determines the normal operation of the whole system. Molten salt is a common heat transfer medium used in tower receivers. However, molten salt is sensitive to solar flux fluctuations because it decomposes when the temperature is above 620°C. Therefore, the steady working of central receivers is threatened by the overheating and decomposition of molten salt (Rodríguez-Sánchez et al., 2014). To increase the safety margin and maintain a high system efficiency, strategies are needed to protect the receiver and allow its operation at various temperatures.

Thermochemical energy storage (TCES) based on metal oxides has the potential to protect molten salt receivers because it can absorb and release heat through redox reactions in the air atmosphere (Aydin et al., 2015). Considerable research has been conducted to develop more effective TCES materials and novel reactors in recent years (Carrillo et al., 2016a). Wang et al. studied the redox performance of iron-manganese oxide particles in a packed-bed solar thermochemical reactor (Wang et al., 2021). A coupling model was also developed to verify and optimize the reactor concept (Wang et al., 2020). For the protection of solar molten salt receivers, redox reactions around 650°C with fast kinetics and robust stability are desired, where an appropriate candidate from metal oxides is still missing (Dizaji and Hosseini, 2018; Pardo et al., 2014; Carrillo et al., 2016b, 2016c; Hamidi et al., 2019; André et al., 2018). Perovskites with an ABO_3 formula are promising candidates because of fast redox kinetics, high oxygen diffusion rates, (Gokon et al., 2019) and favorable cycle repeatability (Vieten et al., 2019). The basic reactions of ABO_3 perovskites can be described by Equations 1 and 2 (Popczun et al., 2020). The working process of the perovskite-type

[1]State Key Laboratory of Clean Energy Utilization, College of Energy Engineering, Zhejiang University, Hangzhou, Zhejiang 310027, China

[2]Qingshanhu Energy Research Center, Zhejiang University, Linan, Hangzhou, Zhejiang 310027, China

[3]State Key Laboratory of Silicon Materials, College of Materials Science and Engineering, Zhejiang University, Hangzhou, Zhejiang 310027, China

[4]Lead contact

*Correspondence: xiaogangtianmen@zju.edu.cn

https://doi.org/10.1016/j.isci.2021.103039

This is an open access article under the CC BY-NC-ND license (http://creativecommons.org/licenses/by-nc-nd/4.0/).

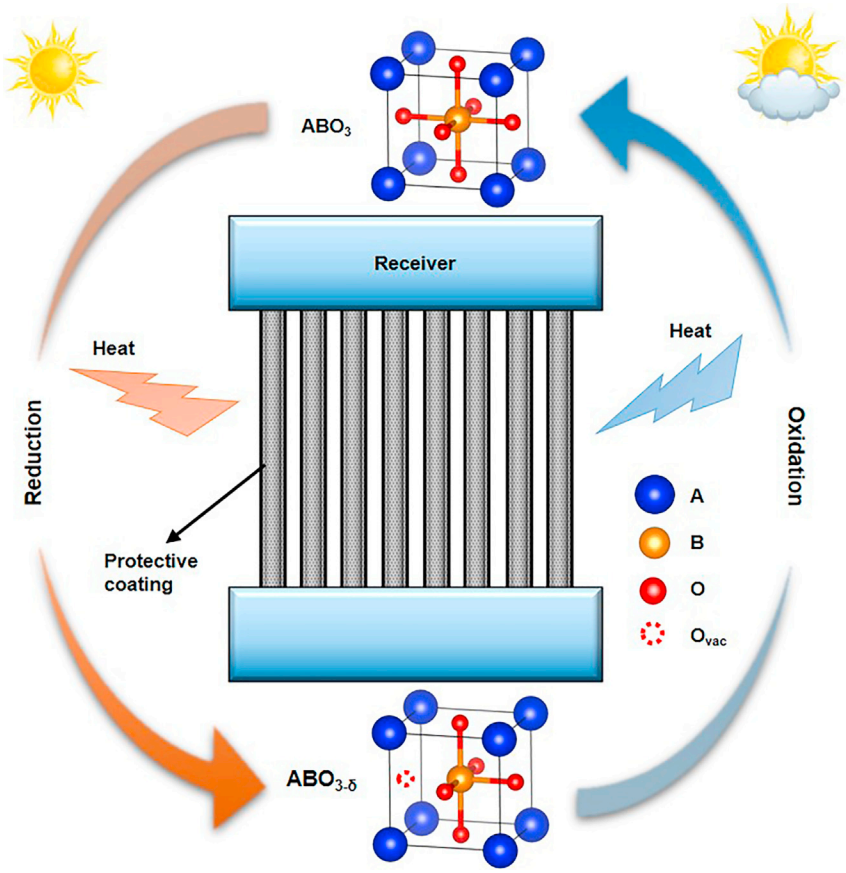

Figure 1. Schematic illustration of thermochemical protective coating for molten salt receivers

The coating undergoes an endothermic reduction reaction under increasing solar flux and absorbs redundant heat from receiver tubes. The coating undergoes an exothermic oxidation reaction under decreasing solar flux and releases heat to receiver tubes.

coating is shown in Figure 1. At high solar flux intensities, the protective coating will undergo a reduction reaction to absorb excess heat and prevent the overheating. At low solar flux intensities, an oxidation reaction will occur in the protective coating to release heat and retard the temperature decrease.

$$\text{Reduction}: ABO_3 \rightarrow ABO_{3-\delta} + \frac{\delta}{2}O_2(g) \quad \text{(Equation 1)}$$

$$\text{Oxidation}: ABO_{3-\delta} + \frac{\delta}{2}O_2(g) \rightarrow ABO_3 \quad \text{(Equation 2)}$$

The A-site cations are usually alkaline metals or rare earth metals with large ionic radius, whereas the B-site is often occupied by transition metals (Scheffe et al., 2013; Babiniec et al., 2016). Substitutions on A or B-sites with different elements enable the regulation of redox properties (Bulfin et al., 2017; Babiniec et al., 2015). Babiniec et al. investigated $La_xSr_{1-x}Co_yMn_{1-y}O_3$ and $La_xSr_{1-x}Co_yFe_{1-y}O_3$ for thermochemical energy storages (Babiniec et al., 2015), which showed that the onset temperature and enthalpy of reduction reactions could be significantly influenced by the crystal structure. However, the significant reduction of La-series perovskites needs relatively low temperature and high oxygen partial pressure. They also explored $CaMnO_3$ by doping Al or Ti at the B-site of $CaMnO_3$ and managed to increase the temperature and enthalpy of the reduction reaction (Babiniec et al., 2015). Imponenti et al. investigated $Ca_{1-x}Sr_xMnO_{3-\delta}$ (x = 0.05 and 0.1) for thermochemical energy storage (Imponenti et al., 2017), where they found low values of Sr-doping at A-site could eliminate the phase decomposition above 1000°C, resulting in a robust stability. These research results indicate perovskites reactivity can be tuned by A or B-site substitution. Zhang et al. provided an experimental assessment of the redox properties of Ba and Sr series perovskites with Fe, Co and Mn incorporated on the B-site (Zhang et al., 2016). $BaCoO_3$ showed the highest O_2 exchange

capacity and reaction enthalpy, whereas $BaMnO_3$ showed poor redox properties under 1050°C. Therefore, Mn element is hypothesized to increase the reduction temperature of $BaCoO_3$ in this study.

Substitutions with a variety of elements will create a large number of candidates, where identifying the optimal material becomes challenging (Scheffe et al., 2013). Thus, it is important to study the underlying mechanism of the substitution effect and build a correlation between microstructures and thermal characteristics. Density functional theory (DFT) can be used as a theoretical instruction for the material design. Several DFT studies have concentrated on the thermochemical properties of perovskites (Merkle et al., 2012; Curnan and Kitchin, 2014). Ezbiri et al. proposed design principles of perovskites for thermochemical oxygen separation (Ezbiri et al., 2015). Their calculation results indicated $BaCoO_3$ and $BaMnO_3$ had too weak and too strong oxygen bindings, respectively, but additional complex perovskites were not discussed in this study. Pavone et al. provided quantum-mechanics-based design principles for solid oxide fuel cell cathode materials (Pavone et al., 2011). They discovered oxygen vacancy formation energies could be influenced by two effects: intrinsic strengths of B-O bonds and intra-atomic exchange energy. However, these calculations were not validated by experimental data.

In this work, oxygen defect engineering via element substitution has been proposed to regulate thermochemical energy storage temperatures. The blank temperature range (530–850°C) was filled by $BaCo_{1-x}Mn_xO_{3-\delta}$ (x = 0–0.4) with a tunable reduction temperature between 426°C and 702°C (see Figure S1). The addition of Mn led to a finer morphology and a higher reaction temperature. The complex perovskites also showed a good cyclability over 100 cycles. To seek a better understanding of the role of Mn substitution, the regulation mechanism was demonstrated through DFT calculations. Moreover, $BaCo_{0.8}Mn_{0.2}O_{3-\delta}$ was tested on a lab-scale receiver, showing a potential to relieve the thermal shock of molten salt receivers. This method can serve as a guideline for the rational design of thermochemical energy storage materials for various solar plants.

RESULTS

Structure and composition

Figure 2A shows the basic structure of $BaCo_{1-x}Mn_xO_3$ perovskites, where x denotes the concentration of Mn elements. XRD was used to identify the crystal structures of as-prepared $BaCo_{1-x}Mn_xO_{3-\delta}$ (x = 0–0.4) samples, as shown in Figure 2B. The coexistence of $BaCoO_3$ and $BaCoO_{2.6}$ crystal phases can be observed, which is related to the preparation conditions. These characteristic perovskite phases are identified as hexagonal structures at room temperature. With the increase of x, two main peaks at 28.5° and 31.5° are observed to shift to lower angles, because larger ionic radius of Mn^{4+} leads to an increase in the lattice constants. EDS mapping was conducted to observe the element distribution in the samples. Taking x = 0.2 as a representative, the Mn element is dispersed uniformly in the matrix of $BaCoO_{3-\delta}$ sample, as shown in Figure S2. The SEM images were taken to better understand the morphology of the synthesized samples. As shown in Figures 2C–2E, the $BaCoO_{3-\delta}$ material forms an agglomeration of small particles, which exhibits a large particle size. With the increase of Mn content, the particles become smaller with a good dispersion property. Therefore, the addition of Mn restrains grain growth, which is favorable for the diffusion of oxygen.

XPS measurement was used to analyze the valence, distribution and relative concentration of surface elements (Nie et al., 2019; Qiu et al., 2020). Figure S3A depicts the XPS survey spectrum of $BaCo_{1-x}Mn_xO_{3-\delta}$ when x = 0.2. The spectrum of Mn2p can be deconvoluted into two doublets, corresponding to Mn^{4+} (642.59 eV, 654.04 eV) and Mn^{3+} (641.27 eV, 653.07 eV), respectively (Uppara et al., 2020). The area ratio of Mn^{4+}/Mn^{3+} is 1.48, indicating Mn^{4+} is dominant in the sample. The O1s spectra of pure and doped samples are compared in Figures S3B and S3C. Each spectrum can be fitted with two oxygen species. The peaks between 528.2 eV and 528.5 eV are associated with lattice oxygen in the perovskites (Cai et al., 2015). The peaks around 530.6 eV are ascribed to adsorbed oxygen species (Cai et al., 2015). After Mn-doping, the ratio of lattice oxygen increases from 18.23% to 25.07%, indicating less oxygen vacancies will be formed. Moreover, the peak of lattice oxygen has shifted to a higher binding energy (528.5 eV), which may be caused by the stronger Mn-O bond.

Thermal characteristics

Figure 3A illustrates the simplified mechanism of redox reactions. Oxygen is released during the reduction and adsorbed during the oxidation, leading to mass change of the sample. TG experiments were performed to investigate the reaction temperatures and thermal characteristics of the complex perovskites.

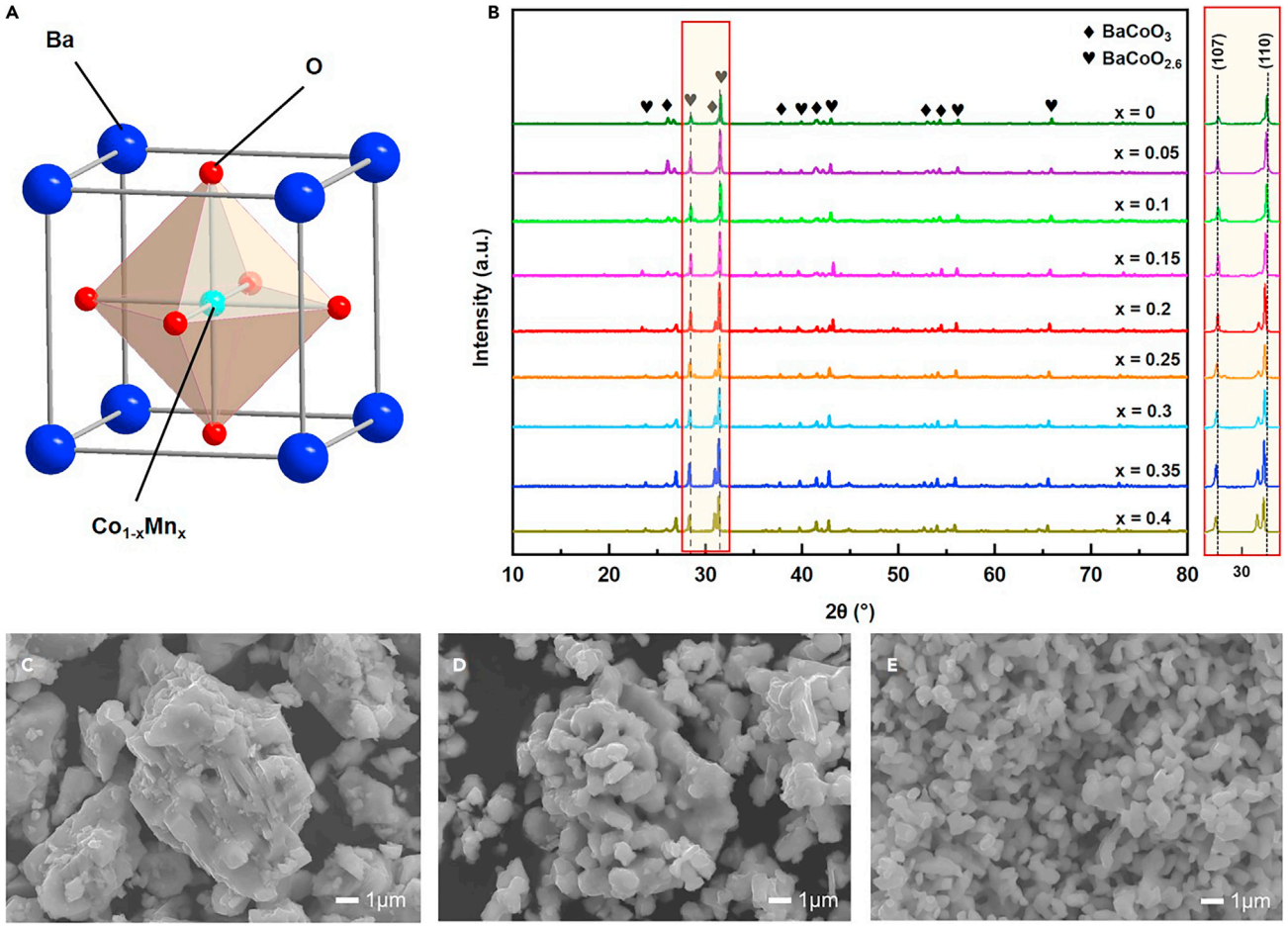

Figure 2. Structure and composition of $BaCo_{1-x}Mn_xO_{3-\delta}$ samples

(A) The basic structure of $BaCo_{1-x}Mn_xO_3$ perovskites.

(B) XRD patterns. Two main peaks at 28.5° and 31.5° are shifted to the lower angle according to local amplification between 25 and 35°.

(C–E) SEM images of $BaCo_{1-x}Mn_xO_{3-\delta}$, where x = 0, 0.2, and 0.4, respectively. See also Figures S2 and S3.

Figure 3B shows the TG curves of $BaCo_{1-x}Mn_xO_{3-\delta}$ (x = 0–0.4). The non-stoichiometry value δ denotes the reaction extent, which can be calculated by Equation 3 (Tang et al., 2010).

$$\delta = \frac{\Delta m}{m_0} \times \frac{M}{M_O} \quad \text{(Equation 3)}$$

Here, Δm is the mass change, m_0 is the initial mass of the sample, M is the molar mass of the sample and M_O is the molar mass of an oxygen atom.

As shown in Figure 3B, each sample shows a reversible redox reaction because of the synthesized perovskite structures. $BaCoO_{3-\delta}$ does not return to the initial mass, which can be attributed to some irreversible mass losses, such as strongly bound water, residual surface carbonates and hydroxides, et al. (Barcellos et al., 2018). The reversibility of $BaCoO_{3-\delta}$ can be confirmed by Figure S4. Notably, the reduction of $BaCoO_{3-\delta}$ seems to have two steps because of the coexistence of $BaCoO_3$ and $BaCoO_{2.6}$ crystal phases. The addition of Mn enhances the phase stability at low temperature, so the doped samples do not show two-step reduction under the test temperature. The XRD patterns of reduced samples can be seen in Figure S5. With the increase of Mn concentration level, the reduction onset temperature T_{re} shows a gradual increase in the range of 426–702°C. Compared with the pure $BaCoO_{3-\delta}$, T_{re} of $BaCo_{0.95}Mn_{0.05}O_{3-\delta}$ rises significantly from 426 to 568°C. In the range of x = 0.05–0.4, T_{re} displays an approximately linear increase with increasing Mn content, as shown in Figure 3C. The relationship of the Mn concentration and the reduction temperature can be described by Equation 4.

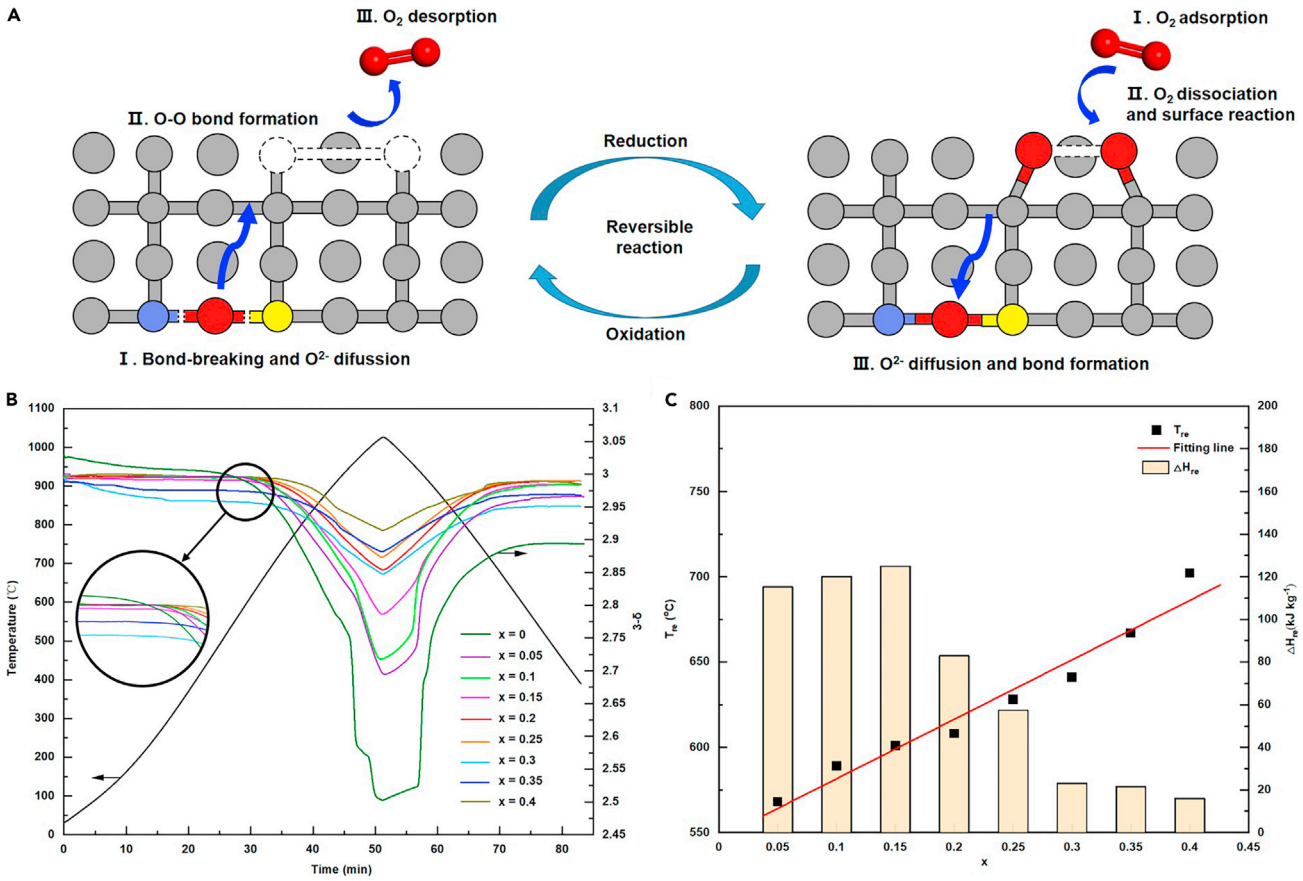

Figure 3. Redox reaction mechanism and thermal characteristics

(A) Schematic illustration of the simplified redox reaction mechanism.

(B) TG curves of $BaCo_{1-x}Mn_xO_{3-\delta}$ (x = 0–0.4).

(C) The fitting line of x and the reduction temperature. The bar chart shows the reduction enthalpy. See also Figures S4 and S5.

$$T_{re} = 349.524x + 546.857 \quad (^{\circ}C) \qquad \text{(Equation 4)}$$

Another crucial parameter for the TES materials is the thermal capacity, i.e., the reduction enthalpy ΔH_{re}, which was measured by differential scanning calorimetry (DSC). ΔH_{re} is expected to increase with the increasing reduction temperature, but the extent of reaction decreases clearly when x varies from 0 to 0.4. The δ_{re} is 0.092 and 0.090 when x = 0.35 and 0.4, respectively, indicating samples with a high Mn content are hard to be reduced under 1050°C. Correspondingly, the heat change is hard to be detected because of the low extent of reaction. It can be seen from Figure 3B that the maximum ΔH_{re} reaches 124.96 kJ kg^{-1} when x = 0.15. After that, the ΔH_{re} tends to decrease rapidly because of the incompleteness of the reaction. The thermal characteristics analyzed by TG and DSC are summarized in Table 1. In addition, the samples with a high Mn concentration show slow reaction kinetics. These results suggest a balance between high reaction temperatures and fast kinetics in the material design.

Cyclic stability

To study the cyclic stability of doped perovskites, all samples were cycled for 120 times between 400 and 1050°C in a tube furnace, where every 20 cycles were chosen as a test point. The redox performance was tested by TG and the results are shown in Figures 4A and 4B. The $BaCo_{1-x}Mn_xO_{3-\delta}$ materials suffer a performance degradation in the first 20 cycles especially at low Mn doping levels. Interestingly, an enhancement of cyclability is obtained when increasing Mn concentration, which may be governed by the morphology. The SEM images were given for a better understanding of the morphology change of the cycled samples. As shown in Figures 4C–4E, the particle sizes become larger compared with fresh samples (Figures 2C–2E), indicating an increase of crystallinity (Zaki et al., 2020). This can also be demonstrated by

Table 1. Thermal characteristics of $BaCo_{1-x}Mn_xO_{3-\delta}$ analyzed by TG and DSC.

x	T_{re} (°C)	δ_{re}	ΔH_{re} (kJ kg^{-1})
0	426	0.500	104.50
0.05	568	0.300	115.21
0.1	589	0.280	120.15
0.15	601	0.220	124.96
0.2	608	0.150	82.95
0.25	628	0.130	57.46
0.3	641	0.110	23.15
0.35	667	0.092	21.55
0.4	702	0.090	16.08

XRD patterns, as shown in Figure 2F. When $x \geq 0.2$, the peaks become narrow over 120 cycles. The XRD patterns of all samples after 120 cycles can be seen in Figure S6, indicating a structural stability. In general, the complex perovskites exhibit a good cyclic stability after 120 thermal cycles, indicating a potential for the long-term thermochemical energy storage.

DFT calculations

The DFT method was used to gain further insights into the mechanism of Mn substitution. After the formation of one oxygen vacancy, two extra charges will transfer from O 2p to 3d orbitals of B-site metals. The Mulliken charges were calculated and averaged for each metal ion, as shown in Table S1. The effective charge of Ba is close to +2 e, whereas the charges of Co and Mn are much smaller than +4 e. This result confirms the covalent nature of B-O bonds, which has also been reported in other works (Goodenough, 1955). After the formation of one oxygen vacancy, Mn obtains a larger electron density than Co. Figure 5A displays the charge density differences at the (300) plane in $BaCo_{0.75}Mn_{0.25}O_3$ after the formation of one oxygen vacancy. It can be seen that the charge transferred to Mn is higher than that of Co, which is consistent with Ezbiri's study (Ezbiri et al., 2015). Total density of states in pure and Mn-doped $BaCoO_3$ models was also calculated, as shown in Figures 5B and 5C. Here, zero corresponds to Fermi level E_F. The bond strength between O and B-site metals can be illustrated by a pseudogap width, namely the distance between peaks on both sides of E_F (Yan and Zhao, 2014). As shown in Figure 5B, the pseudogap width is 1.5 eV in the pure $BaCoO_3$ model. After Mn substitution, the left peak shifts away from E_F and the pseudogap width increases to 2.4 eV, caused by a higher bond strength. In summary, the charge distribution and increased pseudogap width suggest the strength of Mn-O bonds is stronger, leading to a higher reduction temperature.

To have an efficient comparison with the experiments, the models were expanded to 5 × 2×2 supercells with the Mn substitution fraction ranging from 0 to 0.4. As shown in Figure S7, different types of oxygen vacancies have been considered in accordance with the number of neighboring Mn atoms. In general, the E_{vac} near Mn atoms tends to be larger because Mn-O bonds are stronger than Co-O bonds. Figure 5D depicts the averaged E_{vac} versus Mn concentration (x) along with the average B-O bond length. Essentially, the reaction temperature is mainly regulated by the energy required to break B-O bonds, i.e., E_{vac}. Overall, the E_{vac} becomes larger with the increasing x, indicating the oxygen release becomes more difficult. The less content of Mn has an evident effect on the E_{vac}, especially when x = 0.05. The introduction of Mn will lead to different electronic structures and crystal phases. However, the structure tends to be stable with the increase of Mn content, so the effect of Mn substitution becomes small. The E_{vac} is confirmed as an effective parameter for estimating the reduction temperature of perovskite materials, providing a theoretical instruction for the material design in the future.

In addition, transport properties of oxygen vacancies were studied by the transition-state (TS) theory, which was finished in a CASTEP module. An oxygen vacancy was introduced into different sites of the $BaCo_{0.75}Mn_{0.25}O_3$ model as the initial and final structures. The migration paths of the oxygen vacancy are shown in Figures 6A and 6B. The diffusion kinetics of the oxygen vacancy can be inferred by comparing the migration energy across Ba-Co-Ba and Ba-Mn-Ba triangular surfaces. The calculated results are shown in Figures 6C and 6D. To make comparable data, the energy of the initial structure is set to be 0 eV. The

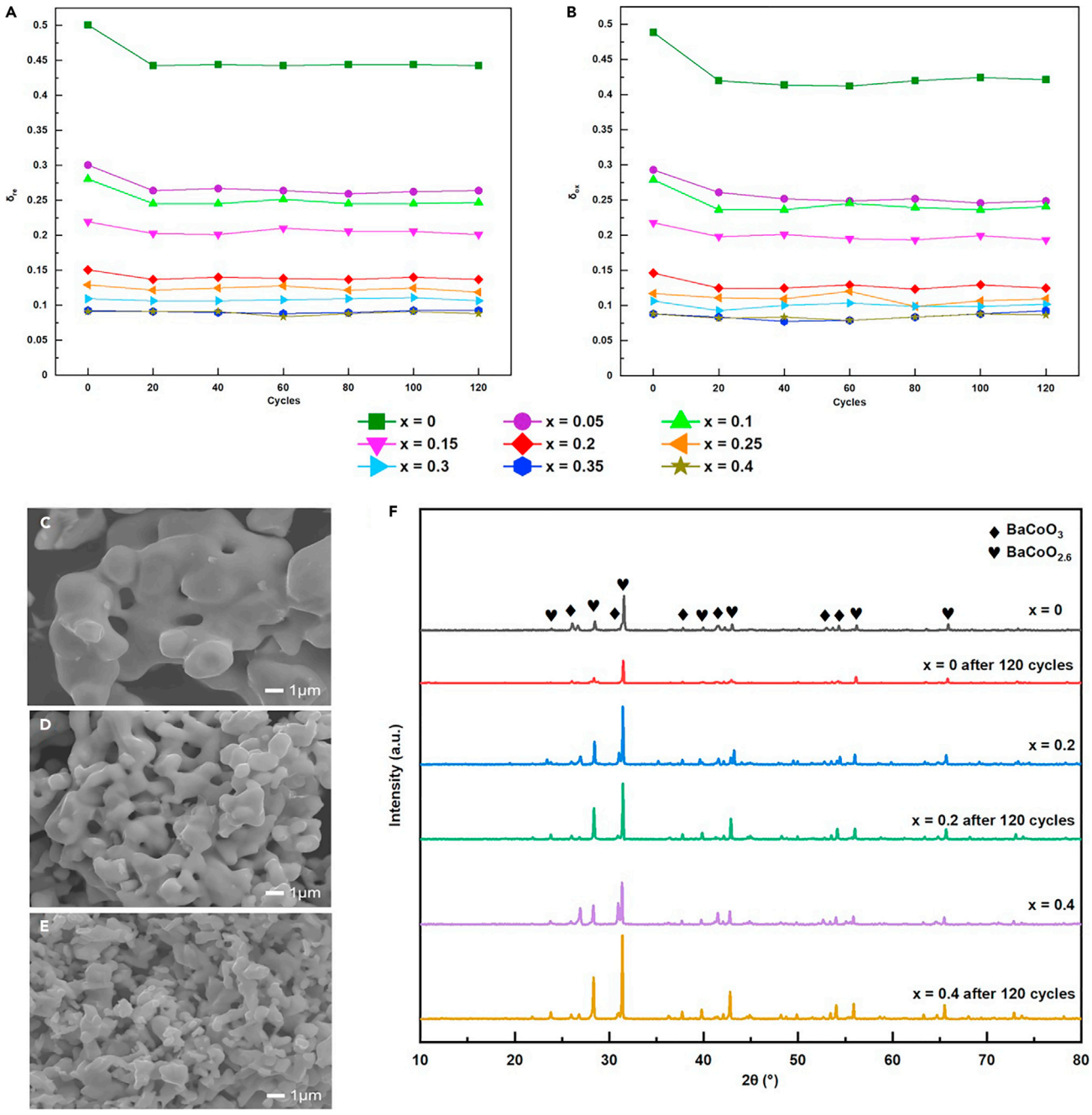

Figure 4. Cyclic stability of $BaCo_{1-x}Mn_xO_{3-\delta}$

(A) Reduction stability of 120 cycles.

(B) Oxidation stability of 120 cycles.

(C–E) SEM images of $BaCo_{1-x}Mn_xO_{3-\delta}$, where x = 0, 0.2, and 0.4, respectively.

(F) XRD patterns of x = 0, 0.2, 0.4 before and after 120 cycles. The narrow peaks indicate an increase of crystallinity after 120 cycles. See also Figure S6.

migration energy across Ba-Co-Ba triangle is 0.2 eV, whereas e the migration energy across Ba-Mn-Ba triangle is about 0.46 eV. The migration barrier is higher around Mn because the electron affinity of Mn is larger than that of Co. This means the reaction kinetics become slower with increasing Mn content, which agrees with experimental results.

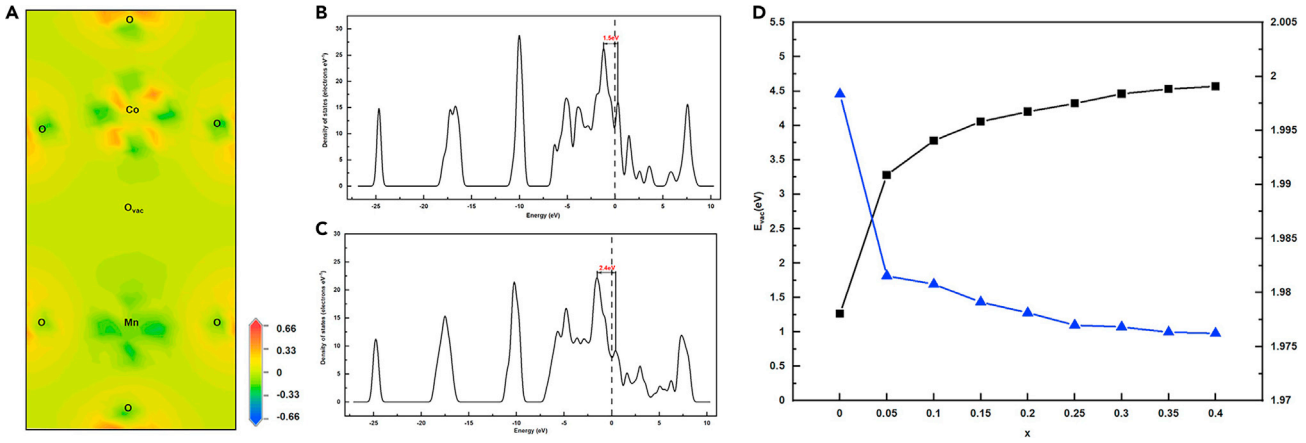

Figure 5. Charge analysis of $BaCo_{1-x}Mn_xO_{3-\delta}$ models

(A) Charge density differences of plane (300) in defective $BaCo_{0.75}Mn_{0.25}O_3$ model (warm color corresponds to positive charge, cool color corresponds to negative charge). According to the depth of the color, Mn obtains a larger electron density than Co.

(B) Total density of states in $BaCoO_3$ model (zero corresponds to Fermi level E_F). The pseudogap width is 1.5 eV.

(C) Total density of states in $BaCo_{0.75}Mn_{0.25}O_3$ model (zero corresponds to Fermi level E_F). The pseudogap width is 2.4 eV.

(D) The averaged E_{vac} along with the B-O bond length as a function of Mn concentration. See also Figure S7 and Table S1.

Lab-scale application

A lab-scale system was built to verify the feasibility of thermochemical protection by $BaCo_{1-x}Mn_xO_{3-\delta}$ (x = 0.15, 0.2, 0.25), as shown in Figure 7A. The control group should be stable under 700°C and have the similar absorptance and thermal conductivity with the test group, as shown in Table S2. In this work, CuO and Mn_2O_3 were chosen as control groups. The solar lamps were used to simulate the solar radiation and the flux density was controlled by changing the numbers of lamps. For simplification, air was chosen as the heat transfer fluid. The top surface of receiver tubes was covered by the coating, so the central temperature of the bottom surface center was measured by a K-type thermocouple with a maximum error of ±2.8°C. The experiment revealed the temperature difference between the top and bottom surfaces of central tubes was about 20°C when the air flow stabilized at 6 $m^3\ h^{-1}$. To simulate a stable operating condition, the temperature of the bottom surface center was heated up to 630°C. After a period of stability, the solar flux was increased by 1.08 W cm^{-2}. The test results are shown in Figure 7B. With the quick increase of radiation intensity, the central temperature of receiver tubes rises dramatically without the protective coating. There is no obvious protective effect for the $BaCo_{0.85}Mn_{0.15}O_{3-\delta}$ coating, whose reduction onset temperature is 610°C according to the TG test. This is possibly because most of the powder has been reduced before the solar flux increases. $BaCo_{0.8}Mn_{0.2}O_{3-\delta}$ and $BaCo_{0.75}Mn_{0.25}O_{3-\delta}$ show similar protective effects, but the temperature curve is smoother with the $BaCo_{0.8}Mn_{0.2}O_{3-\delta}$ coating. The condition under the sudden decrease of solar flux was also considered, as shown in Figure 7C. All three candidates delay the temperature reduction of receiver tubes evidently. Comparatively, the $BaCo_{0.85}Mn_{0.15}O_{3-\delta}$ coating shows a better effect owing to a higher energy storage density. The temperature changing rate of different coatings can be found in Table S3. In general, the $BaCo_{0.8}Mn_{0.2}O_{3-\delta}$ has a good integrative protective performance. In order to verify the stability of the coating, $BaCo_{0.8}Mn_{0.2}O_{3-\delta}$ was applied to a 30 × 30 mm^2 stainless steel plate. After 120 cycles in a tube furnace between 600 and 700°C, an orange peel can be observed, which is mainly caused by the redox reactions. According to ASTM D3359-17, the coating adhesion changes from 4B to 1B. The external appearances can be seen from Figures 7D and 7E. The results demonstrate the protective coating can relieve thermal shock of the receiver effectively, which is favorable for the efficiency enhancement and safe operation in molten salt systems.

DISCUSSION

An active coating based on thermochemical redox reactions has been proposed to protect solar molten salt receivers from solar flux fluctuation. In order to find appropriate metal oxides working in the temperature range of 530–850°C, a method to regulate thermochemical redox temperatures via oxygen defect engineering on perovskites has been investigated by experimental and density functional theory study.

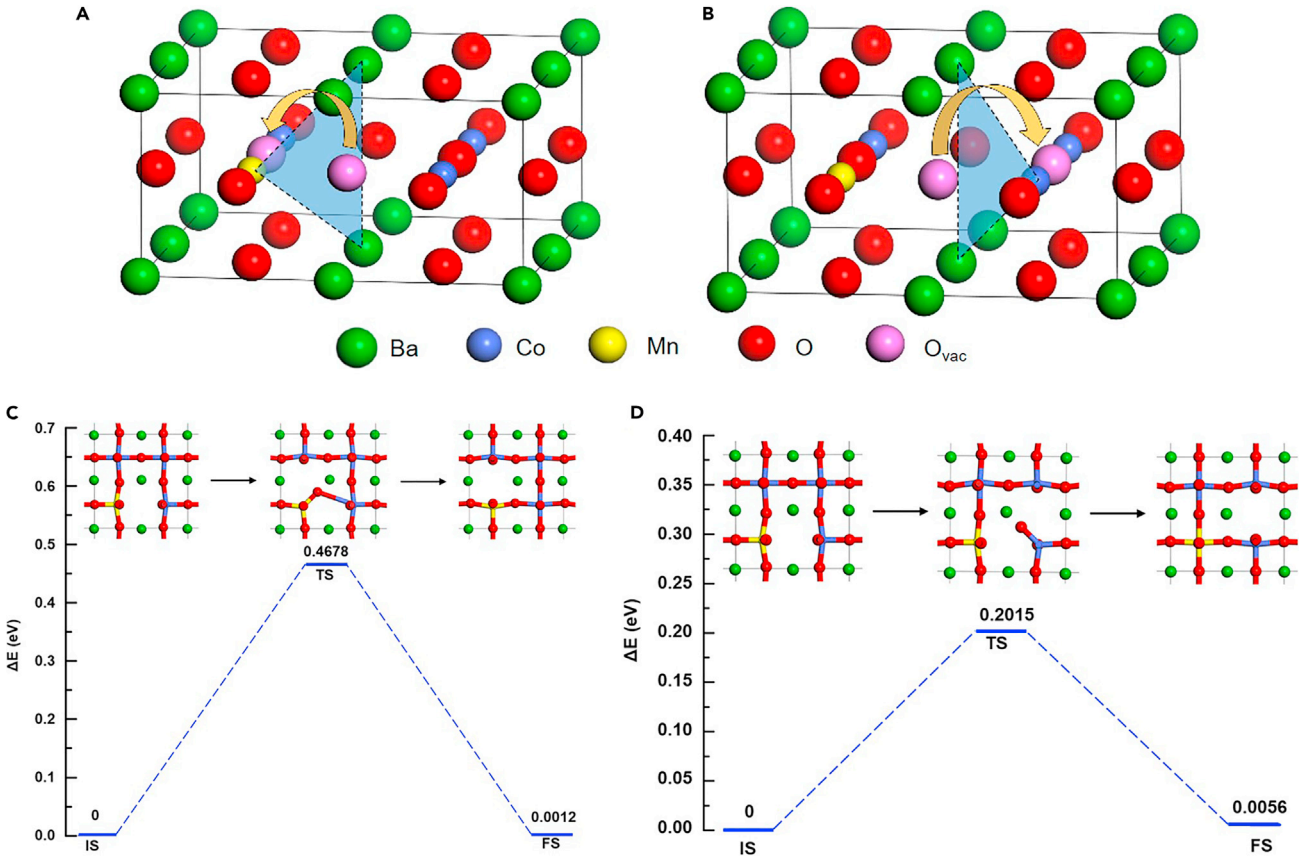

Figure 6. Transport properties of $BaCo_{0.75}Mn_{0.25}O_3$ models

(A) Migration path of oxygen vacancies across Ba-Mn-Ba surface.

(B) Migration path of oxygen vacancies across Ba-Co-Ba surface.

(C) Migration energy profile across Ba-Mn-Ba triangle surface.

(D) Migration energy profile across Ba-Co-Ba triangle surface.

$BaCo_{1-x}Mn_xO_{3-\delta}$ (x = 0–0.4) samples with redox temperatures regulated between 400°C and 700°C were obtained by changing the Mn concentration. With the increasing x, the reduction temperature displayed an approximately linear increase. The samples also showed a good stability (over 90%) after 120 cycles, enabling the long-term application of thermochemical energy storage. DFT calculations were further conducted to understand its detailed mechanism. The reaction temperature was found to be regulated by the formation energy of oxygen vacancy E_{vac}, which was indicated as a theoretical descriptor of the $BaCo_{1-x}Mn_xO_{3-\delta}$. Finally, the protective coating prepared by $BaCo_{0.8}Mn_{0.2}O_{3-\delta}$ was tested on a lab-scale receiver. When the solar flux was increased by 1.08 W cm^{-2}, the temperature changing rate of the tubes decreased from 8.5°C min^{-1} (without coating) to 3°C min^{-1} (with coating) in the first 2 min. Under decreased radiation, the temperature changing rate in the first 2 min was reduced by 3.5°C min^{-1}, which effectively relieved the thermal shock of the receiver. The results are favorable for the safety operation of molten salt systems and can serve as a guideline for the rational design of thermochemical redox reactions for various solar applications.

Limitations of the study

Our work regulates the reaction temperature of $BaCo_{1-x}Mn_xO_{3-\delta}$ in the range of 400–700°C, but the kinetics and energy storage density can be further enhanced. In addition, special additives can be used to increase the thermal conductivity of the coating, making it more compatible with molten salt receivers. At the current stage, different coatings have been tested on a lab-scale receiver. Further scale-up is required in order to estimate the performance of this self-protective coating. The synthetic method and coating method can be improved to adapt with large-scale applications.

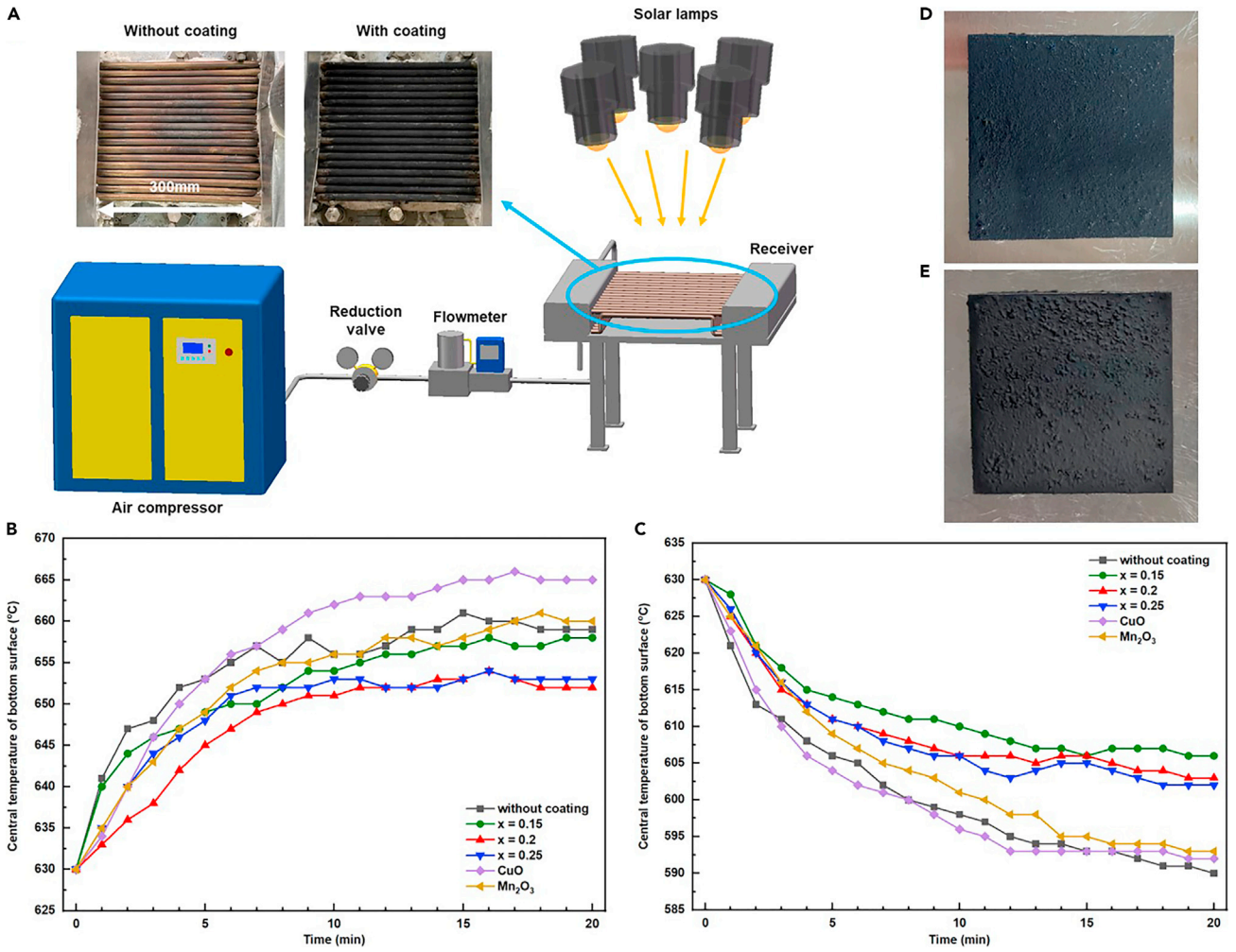

Figure 7. Lab-scale test of thermochemical protective coating

(A) System schematic. The radiation receiving area of receiver tubes is 300 × 300 mm^2.

(B) Central temperature of bottom surface of receiver tubes under increased radiation. x = 0.15, 0.2, 0.25 are test groups. CuO and Mn_2O_3 are control groups.

(C) Central temperature of bottom surface of receiver tubes under decreased radiation. x = 0.15, 0.2, 0.25 are test groups. CuO and Mn_2O_3 are control groups.

(D) The appearance of $BaCo_{0.8}Mn_{0.2}O_{3-\delta}$ coating before 120 cycles.

(E) The appearance of $BaCo_{0.8}Mn_{0.2}O_{3-\delta}$ coating after 120 cycles. See also Tables S2 and S3.

STAR★METHODS

Detailed methods are provided in the online version of this paper and include the following:

- KEY RESOURCES TABLE
- RESOURCE AVAILABILITY
  - Lead contact
  - Materials availability
  - Data and code availability
- METHOD DETAILS
  - Preparation
  - Characterization
  - Coating fabrication
  - Computational methods

SUPPLEMENTAL INFORMATION

Supplemental information can be found online at https://doi.org/10.1016/j.isci.2021.103039.

ACKNOWLEDGMENTS

This work was supported by the Zhejiang Province Natural Science Foundation (No. LR20E060001) and the National Natural Science Foundation of China (No. 51776186 and 51621005).

AUTHOR CONTRIBUTIONS

G.X. conceived and supervised the project. P.Y. and Z.N. performed the experiments and calculations. C.G. contributed to the data analysis. P.Y. and H.X. wrote the paper and K.C. commented on the paper.

DECLARATION OF INTERESTS

The authors declare no competing interests.

Received: May 16, 2021
Revised: August 3, 2021
Accepted: August 21, 2021
Published: September 24, 2021

REFERENCES

André, L., Abanades, S., and Cassayre, L. (2018). Mixed metal oxide systems applied to thermochemical storage of solar energy: benefits of secondary metal addition in Co and Mn oxides and contribution of thermodynamics. Appl. Sci. *8*, 2618.

Aydin, D., Casey, S.P., and Riffat, S. (2015). The latest advancements on thermochemical heat storage systems. Renew. Sustain. Energy Rev. *41*, 356–367.

Babiniec, S.M., Coker, E.N., Miller, J.E., and Ambrosini, A. (2015). Investigation of $La_xSr_{1-x}Co_yM_{1-y}O_{3-\delta}$ (M = Mn, Fe) perovskite materials as thermochemical energy storage media. Sol. Energy *118*, 451–459.

Babiniec, S.M., Coker, E.N., Miller, J.E., and Ambrosini, A. (2016). Doped calcium manganites for advanced high-temperature thermochemical energy storage. Int. J. Energy Res. *40*, 280–284.

Barcellos, D.R., Sanders, M.D., Tong, J.H., McDaniel, A.H., and O'Hayre, R.P. (2018). $BaCe_{0.25}Mn_{0.75}O_{3-\delta}$—a promising perovskite-type oxide for solar thermochemical hydrogen production. Energy Environ. Sci. *11*, 3256–3265.

Bulfin, B., Vieten, J., Agrafiotis, C., Roeb, M., and Sattler, C. (2017). Applications and limitations of two step metal oxide thermochemical redox cycles; a review. J. Mater. Chem. A. *5*, 18951–18966.

Cai, T., Huang, H., Deng, W., Dai, Q.G., Liu, W., and Wang, X.Y. (2015). Catalytic combustion of 1,2-dichlorobenzene at low temperature over Mn-modified Co_3O_4 catalysts. Appl. Catal. B. *166-167*, 393–405.

Carrillo, A.J., Gonzalez-Aguilar, J., Romero, M., and Coronado, J.M. (2019). Solar energy on demand: a review on high temperature thermochemical heat storage systems and materials. Chem. Rev. *119*, 4777–4816.

Carrillo, A.J., Serrano, D.P., Pizarro, P., and Coronado, J.M. (2016a). Understanding redox kinetics of iron-doped manganese oxides for high temperature thermochemical energy storage. J. Phys. Chem. C. *120*, 27800–27812.

Carrillo, A.J., Serrano, D.P., Pizarro, P., and Coronado, J.M. (2016b). Manganese oxide-based thermochemical energy storage: modulating temperatures of redox cycles by Fe–Cu co-doping. J. Energy Storage *5*, 169–176.

Carrillo, A.J., Sastre, D., Serrano, D.P., Pizarro, P., and Coronado, J.M. (2016c). Revisiting the BaO_2/BaO redox cycle for solar thermochemical energy storage. Phys. Chem. Chem. Phys. *18*, 8039–8048.

Curnan, M.T., and Kitchin, J.R. (2014). Effects of concentration, crystal structure, magnetism, and electronic structure method on first-principles oxygen vacancy formation energy trends in perovskites. J. Phys. Chem. C. *18*, 28776–28790.

Dizaji, H.B., and Hosseini, H. (2018). A review of material screening in pure and mixed-metal oxide thermochemical energy storage (TCES) systems for concentrated solar power (CSP) applications. Renew. Sustain. Energy Rev. *98*, 9–26.

D'Olimpio, G., Guo, C., Kuo, C.-N., Edla, R., Lue, C.S., Ottaviano, L., Torelli, P., Wang, L., Boukhvalov, D.W., and Politano, A. (2019). $PdTe_2$ transition-metal dichalcogenide: chemical reactivity, thermal stability, and device implementation. Adv. Funct. Mater. *30*, 1906556.

Ezbiri, M., Allen, K.M., Gàlvez, M.E., Michalsky, R., and Steinfeld, A. (2015). Design principles of perovskites for thermochemical oxygen separation. ChemSusChem *8*, 1966–1971.

Gokon, N., Yawata, T., Bellan, S., Kodama, T., and Cho, H.-S. (2019). Thermochemical behavior of perovskite oxides based on $La_xSr_{1-x}(Mn, Fe, Co)O_{3-\delta}$ and $Ba_ySr_{1-y}CoO_{3-\delta}$ redox system for thermochemical energy storage at high temperatures. Energy *171*, 971–980.

Goodenough, J.B. (1955). Theory of the role of covalence in the perovskite-type manganites [La, M (II)] MnO_3. Phys. Rev. *100*, 564–573.

Hamidi, M., Bayon, A., Wheeler, V.M., Kreider, P., Wallace, M.A., Tsuzuki, T., Catchpole, K., and Weimer, A.W. (2019). Reduction kinetics for large spherical 2:1 iron–manganese oxide redox materials for thermochemical energy storage. Chem. Eng. Sci. *201*, 74–81.

Imponenti, L., Albrecht, K.J., Wands, J.W., Sanders, M.D., and Jackson, G.S. (2017). Thermochemical energy storage in strontium-doped calcium manganites for concentrating solar power applications. Sol. Energy *151*, 1–13.

IRENA (2021). Renewable Power Generation Costs in 2020 (International Renewable Energy Agency)978-92-9260-348-9.

Lewis, N.S. (2016). Research opportunities to advance solar energy utilization. Science *351*, aad1920.

Merkle, R., Mastrikov, Y.A., Kotomin, E.A., Kuklja, M.M., and Maier, J. (2012). First principles calculations of oxygen vacancy formation and migration in $Ba_{1-x}Sr_xCo_{1-y}Fe_yO_{3-\delta}$ Perovskites. J. Electrochem. Soc. *159*, B219–B226.

Muhich, C.L., Ehrhart, B.D., Witte, V.A., Miller, S.L., Coker, E.N., Musgrave, C.B., and Weimer, A.W. (2015). Predicting the solar thermochemical water splitting ability and reaction mechanism of metal oxides: a case study of the hercynite family of water splitting cycles. Energ. Environ. Sci. *8*, 3687–3699.

Nie, X.Y., Zheng, D., Chen, Y., Wang, B.Y., Xia, C., Dong, W.J., Wang, X.Y., Wang, H., and Zhu, B. (2019). Processing SCNT($SrCo_{0.8}Nb_{0.1}Ta_{0.1}O_{3-\delta}$)-SCDC($Ce_{0.8}Sm_{0.05}Ca_{0.15}O_{2-\delta}$) composite into semiconductor-ionic membrane fuel cell (SIMFC) to operate below 500 °C. Int. J. Hydrog. Energy *44*, 31372–31385.

Pardo, P., Deydier, A., Anxionnaz-Minvielle, Z., Rougé, S., Cabassud, M., and Cognet, P. (2014). A review on high temperature thermochemical heat energy storage. Renew. Sustain. Energy Rev. *32*, 591–610.

Pavone, M., Ritzmann, A.M., and Carter, E.A. (2011). Quantum-mechanics-based design principles for solid oxide fuel cell cathode materials. Energy Environ. Sci. *4*, 4933–4937.

Popczun, E.J., Tafen, D.N., Natesakhawat, S., Marin, C.M., Nguyen-Phan, T.-D., Zhou, Y.Y., Alfonso, D., and Lekse, J.W. (2020). Temperature tunability in $Sr_{1-x}Ca_xFeO_{3-\delta}$ for reversible oxygen storage: a computational and

experimental study. J. Mater. Chem. A *8*, 2602–2612.

Qiu, Y.F., Li, H.Z., Liu, Y.H., Chi, B., Pu, J., and Li, J. (2020). Effects of niobium doping on the stability of $SrCo_{0.2}Fe_{0.8}O_{3-\delta}$ cathodes for intermediate temperature solid oxide fuel cells. J. Alloys Compd. *829*, 154503.

Rodríguez-Sánchez, M.R., Sánchez-González, A., Marugán-Cruz, C., and Santana, D. (2014). New designs of molten-salt tubular-receiver for solar power tower. Energy Procedia *49*, 504–513.

Scheffe, J.R., Weibel, D., and Steinfeld, A. (2013). Lanthanum–Strontium–manganese perovskites as redox materials for solar thermochemical splitting of H_2O and CO_2. Energ. Fuel. *27*, 4250–4257.

Tang, Y.H., Zhang, H., Cui, L.X., Ouyang, C.Y., Shi, S.Q., Tang, W.H., Li, H., Lee, J.-S., and Chen, L.Q. (2010). First-principles investigation on redox properties of M-doped CeO_2 (M = Mn, Pr, Sn, Zr). Phys. Rev. B. *82*, 125104.

Uppara, H.P., Pasuparthy, S.J., Pradhan, S., Singh, S.K., Labhsetwar, N.K., and Dasari, H. (2020). The comparative experimental investigations of $SrMn(Co^{3+}/Co^{2+})O_{3\pm\delta}$ and $SrMn(Cu^{2+})O_{3\pm\delta}$ perovskites towards soot oxidation activity. Mol. Catal. *482*, 110665.

Vieten, J., Bulfin, B., Huck, P., Horton, M., Guban, D., Zhu, L.Y., Lu, Y.J., Persson, K.A., Roeb, M., and Sattler, C. (2019). Materials design of perovskite solid solutions for thermochemical applications. Energy Environ. Sci. *12*, 1369–1384.

Wang, B., Li, L.F., Schäfer, F., Pottas, J.J., Kumar, A., Wheeler, V.M., and Lipiński, W. (2021). Thermal reduction of iron–manganese oxide particles in a high-temperature packed-bed solar thermochemical reactor. Chem. Eng. J. *412*, 128255.

Wang, B., Li, L.F., Bader, R., and Lipiński, W. (2020). Thermal model of a solar thermochemical reactor for metal oxide reduction. J. Sol. Energ. Eng. *142*, 051002.

Yan, J., and Zhao, C.Y. (2014). First-principle study of $CaO/Ca(OH)_2$ thermochemical energy storage system by Li or Mg cation doping. Chem. Eng. Sci. *117*, 293–300.

Zaki, A., Gutierrez, A., Schmidt, M., Bielsa, D., Linder, M., and Faik, A. (2020). Investigation of $Ca_{12}Al_{14}O_{33}$ Mayenite for hydration/dehydration thermochemical energy storage. J. Energy Storage *31*, 101647.

Zhang, Z., Andre, L., and Abanades, S. (2016). Experimental assessment of oxygen exchange capacity and thermochemical redox cycle behavior of Ba and Sr series perovskites for solar energy storage. Sol. Energy *134*, 494–502.

STAR★METHODS

KEY RESOURCES TABLE

REAGENT or RESOURCE	SOURCE	IDENTIFIER
Chemicals, peptides, and recombinant proteins		
Barium nitrate	Sinopharm Chemical Reagent Co.,Ltd.	CAS: 10022-31-8
Cobalt nitrate hexahydrate	Shanghai Macklin Biochemical Co.,Ltd.	CAS: 10026-22-9
Manganese nitrate 50% aqueous solution	Sinopharm Chemical Reagent Co.,Ltd.	CAS: 10377-66-9
Citric acid monohydrate	Sinopharm Chemical Reagent Co.,Ltd.	CAS: 5949-29-1
Ethylenediamine tetraacetic acid (EDTA)	Sinopharm Chemical Reagent Co.,Ltd.	CAS: 60-00-4
Ammonia solution	Sinopharm Chemical Reagent Co.,Ltd.	CAS: 1336-21-6
Ethylene glycol	Sinopharm Chemical Reagent Co.,Ltd.	CAS: 107-21-1
Polyvinyl alcohol (PVA)	Shanghai Macklin Biochemical Co.,Ltd.	CAS: 9002-89-5
Software and algorithms		
Materials Studio 8.0	Accelrys Software, Inc.	https://accelrys.com

RESOURCE AVAILABILITY

Lead contact

Further information and requests for resources should be directed to and will be fulfilled by the Lead Contact, Gang Xiao (xiaogangtianmen@zju.edu.cn).

Materials availability

This study did not generate new materials.

Data and code availability

This study did not generate any datasets

METHOD DETAILS

Preparation

A modified Pechini method was used to synthesize the $BaCo_{1-x}Mn_xO_{3-\delta}$ ($x = 0, 0.05, 0.1, 0.15, 0.2, 0.25, 0.3, 0.35, 0.4$). The preparation precursors were $Ba(NO_3)_2$, $Co(NO_3)_2{\cdot}6H_2O$, $Mn(NO_3)_2$, citric acid, EDTA, ammonia solution and ethylene glycol. The mole ratio of citric acid, EDTA and total metal ions was 1.2:0.6:1. Stoichiometric amounts of nitrates, citric acid and EDTA were dissolved in de-ionized water at room temperature. After dripping a certain amount of ethylene glycol, the ammonia solution was used to adjust the pH to 8. Then, the solution was stirred at 80°C for 5 h to obtain a resin, which was dried at 150°C for 12 h and heated at 300°C for 3 h to remove organic impurities. Finally, the samples were calcined at 1000°C for 5 h.

Characterization

The samples were characterized with X-ray diffraction (XRD) on an X-pert Powder X-ray diffractometer. Cu-Kα radiation was used with a 0.02 ° step size. The scanning angle (2θ) ranged from 10° to 80°. X-ray photoelectron spectroscopy (XPS) was carried out at room temperature on a ThermoFisher K-Alpha spectrometer. C 1s was used as a standard peak for energy calibration. A shirley background was removed from Mn 2p scan.

The morphologies of samples before and after cycling were observed by scanning electron microscopy (SEM) on a Hitachi SU3500 scanning electron microscope. The accelerating voltage was 20 kV and the magnification was 5000 times. Transmission electron microscopy (TEM) and energy dispersive spectrometer (EDS) were also performed on a Titan ChemiSTEM to analyze the element distributions.

Thermogravimetric (TG) measurements were performed on a Hitachi STA7200 instrument. The samples with masses of ~20 mg were heated to 1050°C and then cooled to 400°C in air. The heating rate was 20°C min^{-1}. The reaction enthalpies were tested by differential scanning calorimetry (DSC) on a NETZSCH STA 449F3. The DSC accuracy was ≤1%. The operating procures were the same as TG measurements.

The absorptance of powder samples was tested by a Shimadzu UV3600. The wavelength range was 300-2500 nm. The thermal conductivity of powder samples was measured by a Hot Disk TPS2500S.

Coating fabrication

The protective coating was mainly composed of the complex perovskite powder and 20 wt% polyvinyl alcohol (PVA) solution, where PVA was considered as a binder. The mass ratio of perovskite powder and PVA solution was 3:1. The mixture was applied evenly to the top surface of receiver tubes with an average thickness of 250 μm. Then the coating was formed after standing for 2 h. In order to eliminate the influence of PVA decomposition, the receiver was preheated to 300°C for 1 h.

Computational methods

In this work, the DFT calculations were conducted with a CASTEP module in Materials Studio 8.0. The generalized gradient approximation (GGA) with Perdew-Burke-Erzernhof (PBE) type was used for electron exchange-correlation (Muhich et al., 2015; D'Olimpio et al., 2019). As shown in Figure S8, the 2×2×1 supercells with 20 atoms were created and optimized to estimate the substitution effect of Mn element semi-quantitatively. $BaCoO_3$ belonged to the Pm3m (#221) space group with a lattice parameter of a = 3.95 Å (Merkle et al., 2012). The 1×2×2 k-point mesh was created and the energy cut-off was 340 eV. A Mulliken charge analysis was used to evaluate the bond strength, and transition state (TS) search was used to determine the migration ability of oxygen vacancies.

In order to improve the calculation accuracy, the unit cells were then expanded to 5×2×2 supercells. The 1×2×2 k-point mesh was used and the energy cut-off was 570 eV. The configurations of $BaCo_{1-x}Mn_xO_3$ (x = 0-0.4) models with the lowest energy are shown in Figure S9, which enables efficient comparisons with experiments. These stable structures tend to have all the Mn atoms localized in a specific sublattice (Babiniec et al., 2016). The optimized lattice parameters are listed in Table S4.

In this work, an oxygen vacancy was introduced by removing an oxygen atom from the supercell. The oxygen formation energy (E_{vac}) can be calculated using Equation 5 (Yan and Zhao, 2014). E_{vac} is considered as an important parameter of the $BaCo_{1-x}Mn_xO_3$ system. At different Mn concentrations, the positions of oxygen vacancies can be classified by coordinate atoms. For a given concentration, E_{vac} was calculated and averaged for each unique position.

$$E_{vac} = E_{defect} + 1/2E_{O_2} - E_{bulk} \quad \text{(Equation 5)}$$

Here, E_{defect} is the total energy of the supercell with an oxygen vacancy, E_{O_2} is the chemical potential of a free oxygen molecule, and E_{bulk} is the total energy of a defect-free supercell.